Wet-Chemical Processing of Phosphorus Composite Nanosheets for High-Rate and High-Capacity Lithium-Ion Batteries

Zhang, Yanyan; Rui, Xianhong; Tang, Yuxin; Liu, Yaqing; Wei, Jiaqi; Chen, Shi; Leow, Wan Ru; Li, Wenlong; Liu, Yuanjun; Deng, Jiyang; Ma, Bing; Yan, Qingyu; Chen, Xiaodong

2016

https://hdl.handle.net/10356/85102

https://doi.org/10.1002/aenm.201502409

Wet-Chemical Processing of Phosphorus Composite Nanosheets for High-Rate and High-Capacity Lithium-ion Batteries

Yanyan Zhang, Xianhong Rui, Yuxin Tang, Yaqing Liu, Jiaqi Wei, Shi Chen, Wan Ru Leow, Wenlong Li, Yuanjun Liu, Jiyang Deng, Bing Ma, Qingyu Yan,* Xiaodong Chen*

[*]   Dr. Y. Zhang,[+] Dr. X. Rui,[+] Dr. Y. Tang,[+] Dr. Y. Liu, J. Wei, W. R. Leow, W. Li, Y. Liu, J. Deng, Dr. B. Ma, Prof. Q. Yan, Prof. X. Chen
        School of Materials Science and Engineering, Nanyang Technological University, 50 Nanyang Avenue, 639798 Singapore
        E-mail: alexyan@ntu.edu.sg (Q. Y.); chenxd@ntu.edu.sg (X. C.)

        Dr. S. Chen
        School of Physical and Mathematical Sciences, Nanyang Technological University, 21 Nanyang Link, Singapore 637371, Singapore

[+]   These authors contributed equally.

Abstract: Phosphorus-based materials are promising for high-performance lithium-ion batteries (LIBs) application due to its high theoretical specific capacity. Currently, the existing physical methods render great difficulty towards rational engineering on the nanostructural phosphorus or its composites, thus limiting its high-rate LIBs applications. Here, we report, for the first time, a sublimation-induced synthesis of phosphorus-based composite nanosheets by a chemistry-based solvothermal reaction. Its formation mechanism involves solid-vapor-solid transformation driven by continuous vaporization-condensation process, as well as subsequent bottom-up assembly growth. The proof-of-concept LIBs composed of the phosphorus-based nanosheets achieve a high capacity of 630 mAh/g at an ultrahigh current density of 20 A/g, which is attributed to efficient lithium ion diffusion and electron transfer. Such simple sublimation-induced transformation opens up new prospects for rational engineering of phosphorus-based materials for enhancing electrochemical performance.

1. Introduction

From the electrochemical perspective, group V elemental phosphorus (P) is a very promising anode material for high capacity lithium-ion batteries (LIBs) application due to its higher theoretical specific capacity (2595 mAh/g for Li_3P) compared with the commercial graphite materials (372 mAh/g).[1] Among the phosphorus allotropes, red phosphorus is commercially available, chemically stable and easy to handle; hence its derived products have been widely studied for rechargeable batteries application.[1-2] However, bulk or micro-size red P materials suffer from dramatic capacity reduction and poor cyclability with continued usage[1h] due to their electronic insulation ($\sim 10^{-14}$ S/cm)[1f] and irreversible reaction related to the pulverization of particles,[1c, 3] which is caused by drastic volume change (> 300%)[1h] during cycling process. In light of this, black P is an alternative electrode material for high-performance LIBs application due to its high electrical conductivity ($\sim 10^2$ S/cm)[1h, 4] and fast kinetics during the Li^+ intercalating process.[4a, 4c] Nevertheless, the traditional high-pressure method (> 1 GPa, **Scheme 1**a) through a pressure-induced structure-change mechanism is extremely difficult as it relies on specifically designed apparatus under controlled temperature (≥ 200 °C).[4c, 5] Recently, a facile mineralizer-assisted gas-phase transformation method was developed to produce large-size bulk black P.[6] However, the resultant particles by the above approaches are more than tens of micrometers in size,[5a, 6] which renders them unsuitable for high-rate LIBs application. Therefore, material nanostructuring and engineering of the red/black P towards the improvement of electrical/ionic conductivity and the alleviation of volume expansion is desired for high-rate LIBs.[7]

To this end, conductive configurations of nanostructured phosphorus materials (amorphous or red P, P-C composites, and metal phosphide, Scheme 1a)[1d, 1e, 2e, 8] with buffering of volume change are widely explored through mechanical approaches (e.g., hand-grinding, mechanical milling, etc. as shown in Table S1).[1f, 2a, 3, 9] Furthermore, an emerging high energy mechanical milling by generating the sufficient pressure (~ 6 GPa) and

temperature,[1c] (Scheme 1a), could even produce the most thermodynamically stable black P or composites with the particles size down to sub-hundred nanometer, which showed improved LIBs performance.[1c, 1h] Impressively, these nanostructured phosphorus or its composites[1d, 1e, 8] could realize high capacity (> 1000 mAh/g) as well as long-cycling life (>100 cycles) for LIBs. However, these top-down mechanical approaches remain difficult with respect to obtaining large-scale uniform distribution of phosphorus nanostructures, as well as to the building of effective transport pathways for electron transfer and ion diffusion through specific structural engineering, which limits its high-rate LIBs applications (Table S1). In addition, although single or few-layered P nanosheets have been reported for improving LIBs performance, their fabrication process from bulk black P is also complicated: not only is the aforementioned approaches (high-pressure method, gas-phase transformation, etc.) involved, a subsequent liquid exfoliation or scotch-tape delamination is also required. [4b, 6, 10] Herein, it is noted that the existing methods for producing various forms of phosphorus or its composites are based on physical processes. Alternatively, a chemistry-based solvothermal strategy was reported to achieve the uniform nanostructures through a bottom-up approach,[11] in which the small nanoparticles tend to form ordered or disordered agglomerates if the interactive potential exceeds the energy of the thermal vibrations.[12] We foresee the potential on developing a chemical route for the formation of phosphorus or its composites nanostructures via the bottom-up strategy.

In this work, we report, for the first time, a sublimation-induced strategy to synthesize two-dimensional (2D) holey phosphorus-based nanosheets with thin thickness (< 5 nm) via the bottom-up assembly of phosphorus nanodomains under a wet-chemical solvothermal reaction (Scheme 1b). Its formation mechanism involves solid-vapor-solid transformation driven by continuous vaporization-condensation process, as well as subsequent bottom-up assembly growth. The phosphorus-based nanosheets are composited of phosphorus (amorphous-, black- P) and phosphorus oxide, which is formed during the sample preparation

due to the ineluctable oxidation in air. The proof-of-concept LIBs composed of the phosphorus composite nanosheets yielded a high reversible capacity of around 1600 mAh/g at 0.2 A/g, and showed little capacity decrease over 100 cycles. In particular, the electrode materials achieved a high capacity of 630 mAh/g at the high current density of 20 A/g, which could be attributed to the efficient lithium ion diffusion and electron transfer within the holey nanosheets structure. Such protocol will provide new avenues for the rational design of other sublimatable materials systems, opening up new opportunities in the synthesis of advanced functional materials for high-performance energy storage devices.

2. Results and Discussion

Here, to achieve the conditions of the sublimation process for phosphorus materials, a solvothermal reaction (Scheme 1b) was employed to prepare phosphorus nanostructures from bulk red phosphorus. Before reaction, the red P precursor has a particle size around 1~10 μm (**Figure 1**a, Figure S1) with the dark red color. Its X-ray diffraction (XRD) pattern in Figure 1c showed a medium-range ordered structure[2a] with the first sharp diffraction peak at $2\theta = 16°$, corresponding to the amorphous nature of red P materials. After the solvothermal reaction, the resultant solution was observed to be black in color. The well-defined Tyndall effect observed in a dilute solution of the resultant P materials (inset of Figure 1c) indicated the presence of highly monodisperse nanostructures in ethanol. The morphology in Figure 1b confirmed the uniform distribution of phosphorus-based nanostructures in large-scale with the size within 1 μm. After the reaction, the red P underwent structural transformation to form the dominated amorphous P phase with the appearance of weak crystalline black phosphorus peaks (Figure 1c and Figure S2), which was due to insufficient pressure (~50 atm) for the crystallization process of black P.[4a, 5b] The crystalline black P phase is also observed in the intermediate product, which is composed of red- and black- P phase (detailed discussion in Figure S2) during the reaction. The transmission electron microscopy (TEM) images in

4

Figure 1d-e and Figure S3 revealed that uniform 2D phosphorus nanosheets were obtained with in-plane pores of a few nanometers on the surface. The high resolution TEM image in Figure 1f showed that the lamellae is composed of numerous nanodomains with different crystallographic orientations, with the lattice fringes of 0.27 and 0.23 nm corresponding to the (040) and (002) planes of orthorhombic black phosphorus, respectively. The disordered structures without discernible lattice fringe and the crystalline phase co-existed in same plane (Figure S3c-d), which is in agreement with the XRD results. Atomic force microscopy (AFM) measurements (Figure 1g-h) were used to further characterize the dimensions of the as-obtained 2D nanosheets, revealing a lateral size of up to 1.0 μm and thickness of around 0.5 ~ 4 nm. Considering a single atomic layer of phosphorus nanosheet is around 0.5 nm,[4a] this is corresponding to few-layer-thick (1 ~ 8 layers) phosphorus nanosheets are successfully fabricated by our approach.

The phosphorus-based nanosheets were further investigated by X-ray photoelectron spectroscopy (XPS) to understand the surface species. The energy-dispersive X-ray spectroscopy (Figure S4) and XPS spectra (Figure S5) confirmed the final product sample is composed of phosphorus, carbon, and oxygen elements, which is similar to the pristine red P. XPS fine scan (**Figure 2**) revealed the different coordination characteristics of C1s, for the red phosphorus and our phosphorus composite nanosheets. That is, the P-C peak at low binding energy bond[1h] (C1s, Figure 2d) was generated in nanosheets sample, and this broad peak with long tail may be due to the minor charging issue. The formation of this peak is due to the breakup of some P-P bonds since the minor portion of solvent may be decomposed under high temperature and high pressure. Moreover, the O1s peak in phosphorus composite nanosheets (Figure 2e-f) is expected to be generated from both of the surface phosphorus oxide on red phosphorus precursor (Figure 2b-c) and the oxidation of P nanosheets when exposing to the air, while the pure phosphorus phase with P-P bonding (Figure 2d) is generated from red P. The disappearance of –OH species in (Figure 2f) in nanosheets sample is due to the

dehydration of phosphorus at high temperature solvothermal reaction. Herein, according the above characterization, the phosphorus-based composite nanosheets are mainly composed of amorphous- and black- P with the surface phosphorus oxide species (Figure 2), which is due to the ineluctable oxidation of phosphorus nanosheets with air after the wet-chemical reaction, as well as the battery electrode fabrication process. This is consistent with the previous work that the easy oxidation of phosphorus nanostructures in air even in a few minutes.[4b, 13]

To unravel the formation mechanism of the holey phosphorus-based composite nanosheets, the time-dependent morphology evolution was examined. As shown in Scheme 1b, the vessel was filled with pure ethanol and then heated to just the sublimation temperature of red phosphorus, which was determined by the thermogravimetric analysis (TGA, Figure S6) with the appearance of sharp weight loss. The morphology evolutions of phosphorus nanostructure with reaction time are shown in **Figure 3** and Figure S7. Herein, we observed that the porous structure generated from the red P precursor (Figure 3a & Figure S7a) co-exist with trace amount of nanosheets at the short reaction time of 2 h. The pores appeared to be evenly distributed and the average pore size was smaller than 100 nm. When the reaction time was increased to 4 h and 6 h, more pores formed (Figure S7c, e), which could be the result of continuous sublimation of red phosphorus. Also, the emergence of nanosheets could be observed (Figure S7b, d, f), and selected area electron diffraction pattern showed a diffuse ring confirming their amorphous nature. As the time was prolonged to 12 h, the fraction of nanosheets increased (Figure 3b). With further reaction to 24 h, it was observed that the product in the top solution was mainly composed of nanosheets (Figure 3c). The Raman spectrum confirms the successful transformation from red to phosphorus composited nanosheets (Figure 3d) since no characteristic Raman peaks of 351 (B1 fundamental mode), 395 (A1 symmetric stretch motion), 466 cm^{-1} (E1 degenerate mode) for red P[14] was observed, which is due to the thin thickness of the nanosheet[4d] and the surface oxide group in the nanosheets.[4b, 13b]

Based on the comprehensive observation and results obtained, we propose that the formation mechanism of holey phosphorus-based nanosheets (Scheme in Figure 3e-h) involves a solid-vapor-solid transformation and a subsequent bottom-up assembly process. In the mixed system, the critical point f_c (T_{mix}, P_{mix}) can be estimated to be the arithmetic mean of the critical temperatures and pressures of the two components,[15]

$$f_c(T_{mix}, P_{mix}) = f(n_p \cdot T_{cp} + n_e \cdot T_{ce}, n_p \cdot P_{cp} + n_e \cdot P_{ce}) \quad (1)$$

in which, n_p and n_e is the molar fraction of phosphorus and ethanol vapor, respectively; T_{cp} (P_{cp}) and T_{ce} (P_{ce}) are the critical point temperatures (or pressures) of phosphorus and ethanol vapor, respectively. In our system, the thermodynamic contribution from phosphorus vapor was negligible as the molar fraction of phosphorus was very small compared to that of ethanol solvent (1:343). According to our experiments, the isothermal system was stable at a pressure of ~ 50 atm and a temperature of 400 ℃, which was near the supercritical regime (T_c = 241 ℃, T_p = 62 atm, Figure S8).[16] As the reaction pressure and temperature rose inside the autoclave, the reaction process is initially dominated by evaporation. The vaporization-condensation process inside the closed system are discussed in Supporting Information. According to Hertz-Knuden-Langmuir equation,[15, 17] the kinetics for vaporization rate of phosphorus can be determined by vapor pressure:

$$J_n = \alpha_v (P_E - P_o)(2\pi m k T)^{-\frac{1}{2}} \quad (2)$$

where J_n is the net flux, α_v is the vaporization coefficient, P_E and P_o is equilibrium vapor pressure and steady-state pressure at temperature T. Initially, the red phosphorus particles initiated evaporation to form phosphorus vapor both inside and outside of the particles (Figure 3e), leaving behind a porous structure within the particles at the bottom of the solution (Figure S7), even at the short reaction time of 2 h (Figure 3a). As evaporation continued, vapor density would increase, leading to the increase of condensation rate. Thus, the net flux of evaporation (J_n) would gradually decrease to zero according to equation (2). With the

increase in reaction temperature, a new equilibrium state would be achieved with greater rates of evaporation and condensation, and thus a greater equilibrium vapor pressure would be built up (Figure 3f). After the pressure became saturated (~50 atm) at 400 °C, the ethanol solution would be close to a supercritical fluid, forming a homogenous ethanol/phosphorus system (Figure 3g). This essential dynamic equilibrium state in the evaporation-condensation process of phosphorus would promote continuous evaporation from the solid state into the vapor regime, and subsequently the condensation of the vapor molecules into ethanol. The continuous solid-vapor-solid transformation would induce the formation of critical nuclei of isolated phosphorus nanodomains, which would act as the source for the nucleation of phosphorus nanosheets formed at the initial stage. The nanodomains would tend to form the nanosheets structure via the bottom-up assembly process[11a] (Figure 3g-h), in which the small nanodomains tended to form ordered agglomerates (nanosheets) when the interactive potential exceeded the energy of the thermal vibrations.[12] The formation of nanosheet structure may be due to strong in-plane bonding and weak Van der Waals inter-planar interactions, which is similar to graphite-like layered material in which individual atomic layers are stacked together.[4b] Indeed, we observed that phosphorus nanodomains co-existed with nanosheets through AFM characterization (Figure S9). As expected, the time-dependent morphology study (Figure 3, and Figure S7) also revealed that the dynamic growth yielding of phosphorus nanosheets with time. Furthermore, the more thermal-stable condensed nanosheets were likely to re-evaporate from some active surface sites at the sublimation temperature, thus leaving nanopores in the nanosheets (Figure 3h and Scheme 1b). Interestingly, with this unique solid-vapor-solid sublimation process, we also demonstrated the feasible preparation of the phosphorus nanosheets on the graphene oxide nanosheets (Figure S10-11), as well as the metal phosphide (Ni_xP, Cu_xP, etc.) on the nickel or copper foam by this solvothermal reaction.

8

As a proof-of-concept for the potential LIBs application of the produced 2D nanosheets, the electrochemical performance of the phosphorus-based nanosheets electrodes are evaluated. The cycling performance of the phosphorus-based nanosheets and red P is shown in **Figure 4**. For the bulk red P electrodes (Figure 4a-b), the first discharge capacity was around 880 mAh/g and dropped to 100 mAh/g after 10 cycles, which was caused by mechanical cracking and crumbling due to large volume change during the charging/discharging process.[1c] For the nanosheets electrode, the problem of volume expansion was alleviated, resulting in an enhancement of the charge/discharge cyclability. The assembled cells exhibited high first cycle discharge and charge capacities of around 2696 and 1969 mAh/g (Figure 4a), respectively, at a current density of 0.2 A/g. The capacity loss in the first cycle could be attributed to the irreversible reactions (e.g., decomposition of electrolyte) to form a solid electrolyte interphase (SEI) film, which is a common character for LIB anodes in the first cycle.[18] It was observed that the difference between the discharge and charge capacities decreased with the increment of cycle number as the Coulombic efficiency increased to over 94% after the 3rd cycle, and that the discharge capacity remained as high as 1683 mAh/g after 100 cycles (Figure 4a). Different from the crystalline phosphorus materials with a steady reaction plateau,[1c, 4c] the redox behaviour for our phosphorus-based nanosheets shows a continuous slope profile with slightly higher working potential (Figure 4c-d). That is, a continuous reduction potential region below 1.0 V (with the oxidation peak at ca. 0.1, 1.1 V) and a stable reduction peak at ca. 1.8 V (with oxidation peak at 2.3 V) are observed. Herein, the lithiation mechanism for the phosphorus-based nanosheets is proposed as follows. Firslty, the continuous reduction region (below 1.0 V) is due to the lithiation process into amophorus nature of phosphorus nanosheets with small portion of black P, as well as the enhanced interfacial lithium storage in ultrathin phosphorus nanosheets (i.e., large surface area) with the capacitive effect. Moreover, the amorphous phosphorus characteristics can allow Li ions to be inserted from randomly oriented directions. These

9

characterstics are important for the high rate LIBs application. Secondly, the reversible high redox potential is due to lithiation/de-lithiation of surface phosphorus oxide in the phosphorus-based nanosheets.[1d, 1e, 4a, 19] Such charge/discharge behaviour transform is very similar to that of other two-dimensional nanosheets materials (metal dichalcogenide, graphene oxide, etc.).[20] Generally, bulk pristine materials are lithiated/de-lithiated at low potential with a flat plateau, while after exfoliation, the ultrathin nanosheets show sloping voltage curves with higher lithiation potential like graphene oxides.[20b-f]

To verify the possibility of employing the phosphorus composite nanosheets electrode for LIBs application at high current density, the rate performance was evaluated (**Figure 5**a). When the current density increased from 0.5 to 20 A/g, the discharge capacity decreased monotonically from 1600 to 630 mAh/g, which is one of the best performance for the phosphorus nanostructured or composites anode for LIBs application at high rates (Table S1). The discharge capacity then increased back to 1400 mAh/g when the current rate returns to 0.5 A/g, and maintained about 87.5% of the initial capacity, which meant that the electrode could reversibly charge/discharge at high current density. The large capacity retention and high-rate capability was due to the the significant decrease of Li^+ ion diffusion length and low internal/charge-transfer resistance (Figure 5b) in the phosphorus-based nanosheets (Figure 5c) compared to that of bulk electrodes. As shown in Figure 5b the impedance spectrum, the internal resistance and ionic charge-transfer resistance were only 7.2 and 65.8 Ω for the phosphorus-based nanosheets electrodes, respectively. In addition, the phosphorus nanosheets have a high Brunauer–Emmett–Teller (BET) surface area around 87 m^2/g while the commercial red P only has a small surface area lower than 1 m^2/g (Figure S12). Thus, the porous nanosheets electrode permitted high contact area with the electrolyte and hence high Li^+ flux across the interface.[19a, 21] In particular, the nanopores in the holey phosphorus sheets were large enough to function as lithium ion reservoirs for neighboring layers of phosphorus, thus greatly speeding up the ion transport across the entire film and facilitating ion access to

the entire surface area (Figure 5c). The characteristic time constant (t) for ionic diffusion is proportional to the square of the diffusion length (L) and inversely proportional to diffusivity (D), as described by the equation of $t \approx L^2/D$. By assuming that red and phosphorus-based nanosheets exhibit similar ionic diffusivity, the diffusion time for nanosheets electrode was more than 5 orders of magnitude lower than that of corresponding bulk materials. According to our calculated value of ionic conductivity for phosphorus composite materials ($10^{-13}\sim10^{-12}$ cm^2/s) by galvanostatic intermittent titration technique (GITT)[22] method (detailed discussion in Figure S13), the diffusion time would be about 0.25~2.5 s within 5 nm thickness of nanosheets. This meant that the holey phosphorus-based nanosheets electrodes possessed fast lithiation kinetics, which enabled excellent rate performance at high current density.

3. Conclusion

In summary, we demonstrated a sublimation-induced transformation method to prepare few-layer-thick (< 8 layers) phosphorus-based nanosheets composited of phosphorus materials (amorphour-, black- P) and phosphorus oxide from their bulk red phosphorus precursors. When the thin phosphorus-based nanosheets was employed as anode in LIBs application, remarkable high-rate performance was achieved, which was due to the short charge diffusion length within the thin holey phosphorus nanosheets (< 4 nm), as well as the alleviation of large volume expansion as compared to that of bulk phosphorus electrode. Such 2D phosphorus nanosheets are extremely promising for next-generation LIBs application; the unique structure not only exhibits potential in fulfilling the great demand for high energy and power density LIBs, but is also attractive for further applications in electronic and optoelectronic devices.

4. Experimental Section

Preparation of phosphorus-based nanosheets: In a typical synthesis, 0.5 g of commercial red phosphorus powder was dispersed into 50 mL of ethanol, and then transferred into 200 mL stainless-steel high pressure reactor. The reaction temperature was set at 400 $^\circ$C with the reaction time ranging from 2 to 24 h. The vessel pressure would build up around ~ 50 bar. After the reaction, the phosphorus product/ethanol solution was sonicated for half hour. After the sedimentation, the nanosheets samples from the top ethanol solution (seperating out the bulk phosphorus or its composite materials) was centrifuged at 10,000 rpm, and then re-disperses in ethanol again to avoid the potential oxidation for the materials characterization. The yileding of nanosheets sample was around 30%. For the battery assembly, the nanosheets were directly dried in vacuum at 100 $^\circ$C for 2 h for the battery electrode preparation.

Materials characterization: The powder X-ray diffraction (XRD) patterns were obtained on a Shimadzu 6000 X-ray diffractometer equipped with a Cu Kα (λ=1.54178 Å) source. The morphology and microstructure of the as-synthesized samples were investigated by field emission scanning electronic microscopy (FESEM; JEOL JSM-7600F) and transmission electron microscopy (TEM; JEOL, JEM-2010). EDX attached to the FESEM was used for the analysis of the component elements. Atomic force microscopy (AFM) (Digital Instruments) was used to determine the thicknesses of resulted phosphorus nanosheets. X-ray photoelectron spectroscopy (XPS) spectra were measured using monochromatic X-ray source (1486.7eV, SPECS) and an electron analyzer (EA125, Omicron) with base pressure better than 1×10^{-9} torr. The XPS source with a resolution of 0.3 ~ 0.5 eV and the spectra were calibrated with the C1s peak at 284.5 eV as an internal standard. Thermogravimetric analysis (TGA) was carried out on a TA Instrument Q500 Thermogravimetric Analyzer at a heating rate of 10 $^\circ$C/min up to 800 $^\circ$C under N_2 atmosphere. The Raman spectroscopy was conducted on a WITec CRM200 confocal Raman microscopy system at room temperature with the excitation line of 488 nm and an air cooling charge coupled device as the detector

(WITec Instruments Corp, Germany). The Raman band of Si at 520 cm^{-1} was used as a reference to calibrate the spectrometer.

Electrochemical Measurement: The electrochemical performance was investigated using coin-type cells (CR 2032) with lithium metal as the counter and reference electrodes. The electrodes were fabricated by mixing of 70 wt% phosphorus nanosheets with single wall carbon nanotube (20 wt%) and polyvinylidene fluoride (PVDF, 10 wt%) in n-methyl-2-pyrrolidone (NMP) solvent, and then pasted onto the copper foils. The red phosphorus electrode was prepared with the same approach. The mass loading was around 1.0 mg. Lithium foils were used as anodes and the electrolyte solution was made of 1 M LiPF$_6$ in ethylene carbonate (EC)/diethyl carbonate (DEC) (1/1, w/w). The cells were assembled in a glove box with oxygen and water contents below 1.0 and 0.5 ppm, respectively. Charge/discharge cycles of phosphorus materials/Li half-cell were tested between 0.1 and 3.0 V vs Li$^+$/Li at varied current densities with a NEWARE battery tester. Also, by the same battery tester, the galvanostatic intermittent titration technique (GITT) for the determination of lithium ion diffusion coefficient was employed as a pulse of 0.05 mA for 20 min and with 120 min interruption between each pulse.

Reference
[1] a) A. Vlad, N. Singh, C. Galande, P. M. Ajayan, *Adv. Energy Mater.* **2015**, 5, 1402115; b) A. S. Arico, P. Bruce, B. Scrosati, J. M. Tarascon, W. Van Schalkwijk, *Nat. Mater.*

2005, 4, 366; c) C. M. Park, H. J. Sohn, *Adv. Mater.* **2007**, 19, 2465; d) J. F. Qian, X. Y. Wu, Y. L. Cao, X. P. Ai, H. X. Yang, *Angew. Chem. Int. Ed.* **2013**, 52, 4633; e) Y. Kim, Y. Park, A. Choi, N.-S. Choi, J. Kim, J. Lee, J. H. Ryu, S. M. Oh, K. T. Lee, *Adv. Mater.* **2013**, 25, 3045; f) J. Song, Z. Yu, M. L. Gordin, S. Hu, R. Yi, D. Tang, T. Walter, M. Regula, D. Choi, X. Li, A. Manivannan, D. Wang, *Nano Lett.* **2014**, 14, 6329; g) N. Nitta, G. Yushin, *Part. Part. Syst. Charact.* **2014**, 31, 317; h) J. Sun, G. Zheng, H.-W. Lee, N. Liu, H. Wang, H. Yao, W. Yang, Y. Cui, *Nano Lett.* **2014**, 14, 4573; i) N.-S. Choi, Z. Chen, S. A. Freunberger, X. Ji, Y.-K. Sun, K. Amine, G. Yushin, L. F. Nazar, J. Cho, P. G. Bruce, *Angew. Chem. Int. Ed.* **2012**, 51, 9994; j) Q.-F. Li, C.-G. Duan, X. G. Wan, J.-L. Kuo, *J. Phys. Chem. C* **2015**, 119, 8662; k) J. Cabana, L. Monconduit, D. Larcher, M. R. Palacín, *Adv. Mater.* **2010**, 22, E170; l) Y. Wang, J. Yi, Y. Xia, *Adv. Energy Mater.* **2012**, 2, 830; m) M. G. Kim, J. Cho, *Adv. Funct. Mater.* **2009**, 19, 1497; n) T.-H. Kim, J.-S. Park, S. K. Chang, S. Choi, J. H. Ryu, H.-K. Song, *Adv. Energy Mater.* **2012**, 2, 860.

[2] a) J. Qian, D. Qiao, X. Ai, Y. Cao, H. Yang, *Chem.Commun.* **2012**, 48, 8931; b) C. Marino, A. Debenedetti, B. Fraisse, F. Favier, L. Monconduit, *Electrochem. Commun.* **2011**, 13, 346; c) M. Nagao, A. Hayashi, M. Tatsumisago, *J. Power Sources* **2011**, 196, 6902; d) M. C. Stan, J. v. Zamory, S. Passerini, T. Nilges, M. Winter, *J.Mater. Chem. A* **2013**, 1, 5293; e) L. Pei, Q. Zhao, C. Chen, J. Liang, J. Chen, *ChemElectroChem* **2015**, 2, 1652; f) Y. Kim, K.-H. Ha, S. M. Oh, K. T. Lee, *Chem. Eur. J.* **2014**, 20, 11980.

[3] W.-J. Li, S.-L. Chou, J.-Z. Wang, H.-K. Liu, S.-X. Dou, *Nano Lett.* **2013**, 13, 5480.

[4] a) H. Liu, Y. Du, Y. Deng, P. D. Ye, *Chem. Soc. Rev.* **2015**, 2732; b) L. Li, Y. Yu, G. J. Ye, Q. Ge, X. Ou, H. Wu, D. Feng, X. H. Chen, Y. Zhang, *Nat. Nanotech.* **2014**, 9, 372; c) L.-Q. Sun, M.-J. Li, K. Sun, S.-H. Yu, R.-S. Wang, H.-M. Xie, *J. Phy. Chem. C* **2012**, 116, 14772; d) Z. Yang, J. Hao, S. Yuan, S. Lin, H. M. Yau, J. Dai, S. P. Lau, *Adv. Mater.* **2015**, 27, 3748.

[5] a) P. W. Bridgman, *J. Am. Chem. Soc.* **1914**, 36, 1344; b) J. C. Jamieson, *Science* **1963**, 139, 1291.

[6] a) L. Chen, G. Zhou, Z. Liu, X. Ma, J. Chen, Z. Zhang, X. Ma, F. Li, H.-M. Cheng, W. Ren, *Adv. Mater.* **2015**, 10.1002/adma.201503678; b) S. Lange, P. Schmidt, T. Nilges, *Inorg. Chem.* **2007**, 46, 4028.

[7] a) K. Kang, Y. S. Meng, J. Bréger, C. P. Grey, G. Ceder, *Science* **2006**, 311, 977; b) B. Kang, G. Ceder, *Nature* **2009**, 458, 190; c) D.-J. Xue, S. Xin, Y. Yan, K.-C. Jiang, Y.-X. Yin, Y.-G. Guo, L.-J. Wan, *J. Am. Chem. Soc.* **2012**, 134, 2512; d) Y.-Q. Wang, L. Gu, Y.-G. Guo, H. Li, X.-Q. He, S. Tsukimoto, Y. Ikuhara, L.-J. Wan, *J. Am. Chem. Soc.* **2012**, 134, 7874; e) H. Wu, G. Chan, J. W. Choi, I. Ryu, Y. Yao, M. T. McDowell, S. W. Lee, A. Jackson, Y. Yang, L. B. Hu, Y. Cui, *Nat. Nanotech.* **2012**, 7, 309; f) J. Y. Wang, N. L. Yang, H. J. Tang, Z. H. Dong, Q. Jin, M. Yang, D. Kisailus, H. J. Zhao, Z. Y. Tang, D. Wang, *Angew. Chem. Int. Ed.* **2013**, 52, 6417; g) A. L. M. Reddy, S. R. Gowda, M. M. Shaijumon, P. M. Ajayan, *Adv. Mater.* **2012**, 24, 5045; h) B. Koo, H. Kim, Y. Cho, K. T. Lee, N. S. Choi, J. Cho, *Angew. Chem. Int. Ed.* **2012**, 51, 8762; i) C. B. Zhu, X. K. Mu, P. A. van Aken, Y. Yu, J. Maier, *Angew. Chem. Int. Ed.* **2014**, 53, 2152; j) W. Wei, S. Yang, H. Zhou, I. Lieberwirth, X. Feng, K. Müllen, *Adv. Mater.* **2013**, 25, 2909; k) Y. Zhao, J. Feng, X. Liu, F. Wang, L. Wang, C. Shi, L. Huang, X. Feng, X. Chen, L. Xu, M. Yan, Q. Zhang, X. Bai, H. Wu, L. Mai, *Nat. Commun.* **2014**, 5, 4565; l) Y. Gong, S. Yang, Z. Liu, L. Ma, R. Vajtai, P. M. Ajayan, *Adv. Mater.* **2013**, 25, 3979; m) P. Simon, Y. Gogotsi, B. Dunn, *Science* **2014**, 343, 1210; n) V. Augustyn, J. Come, M. A. Lowe, J. W. Kim, P.-L. Taberna, S. H. Tolbert, H. D. Abruña, P. Simon, B. Dunn, *Nat. Mater.* **2013**, 12, 518; o) A. Bhaskar, S. Krueger, V. Siozios, J. Li, S. Nowak, M. Winter, *Adv. Energy Mater.* **2015**, 5, 1401156.

[8]   a) W. Li, S.-L. Chou, J.-Z. Wang, J. H. Kim, H.-K. Liu, S.-X. Dou, *Adv. Mater.* **2014**, 26, 4037; b) Y. Kim, Y. Kim, A. Choi, S. Woo, D. Mok, N.-S. Choi, Y. S. Jung, J. H. Ryu, S. M. Oh, K. T. Lee, *Adv. Mater.* **2014**, 26, 4139; c) N. Yabuuchi, Y. Matsuura, T. Ishikawa, S. Kuze, J.-Y. Son, Y.-T. Cui, H. Oji, S. Komaba, *ChemElectroChem* **2014**, 1, 580; d) J. Qian, Y. Xiong, Y. Cao, X. Ai, H. Yang, *Nano Lett.* **2014**, 14, 1865; e) Y. Zhu, Y. Wen, X. Fan, T. Gao, F. Han, C. Luo, S.-C. Liou, C. Wang, *ACS Nano* **2015**, 9, 3254; f) Z. Yu, J. Song, M. L. Gordin, R. Yi, D. Tang, D. Wang, *Adv. Sci.* **2015**, 2, 1400020; g) M. C. Stan, R. Klöpsch, A. Bhaskar, J. Li, S. Passerini, M. Winter, *Adv. Energy Mater.* **2013**, 3, 231; h) X. Fan, J. Mao, Y. Zhu, C. Luo, L. Suo, T. Gao, F. Han, S.-C. Liou, C. Wang, *Adv. Energy Mater.* **2015**, 5, 1500174.

[9]   a) L. Wang, X. He, J. Li, W. Sun, J. Gao, J. Guo, C. Jiang, *Angew. Chem. Int. Ed.* **2012**, 51, 9034; b) W. Li, Z. Yang, Y. Jiang, Z. Yu, L. Gu, Y. Yu, *Carbon* **2014**, 78, 455; c) C. Marino, L. Boulet, P. Gaveau, B. Fraisse, L. Monconduit, *J. Mater. Chem.* **2012**, 22, 22713.

[10]   a) J. R. Brent, N. Savjani, E. A. Lewis, S. J. Haigh, D. J. Lewis, P. O'Brien, *Chem. Commun.* **2014**, 50, 13338; b) P. Yasaei, B. Kumar, T. Foroozan, C. Wang, M. Asadi, D. Tuschel, J. E. Indacochea, R. F. Klie, A. Salehi-Khojin, *Adv. Mater.* **2015**, 1887; c) J. D. Wood, S. A. Wells, D. Jariwala, K.-S. Chen, E. Cho, V. K. Sangwan, X. Liu, L. J. Lauhon, T. J. Marks, M. C. Hersam, *Nano Lett.* **2014**, 14, 6964.

[11]   a) M. Choucair, P. Thordarson, J. A. Stride, *Nat. Nanotech.* **2009**, 4, 30; b) J. M. Tour, *Nature* **2014**, 512, 30; c) J. R. Sanchez-Valencia, T. Dienel, O. Groning, I. Shorubalko, A. Mueller, M. Jansen, K. Amsharov, P. Ruffieux, R. Fasel, *Nature* **2014**, 512, 61.

[12]   A. K. Boal, F. Ilhan, J. E. DeRouchey, T. Thurn-Albrecht, T. P. Russell, V. M. Rotello, *Nature* **2000**, 404, 746.

[13]   a) L. Wang, Z. Sofer, M. Pumera, *ChemElectroChem* **2015**, 2, 324; b) A. Favron, E. Gaufrès, F. Fossard, P. L. Lévesque, A.-L. Phaneuf-L'Heureux, A. L. N. Y. Tang , R. Leonelli, S. Francoeur, R. Martel, **2014**, arXiv:1408.0345.

[14]   E. N. Rissi, E. Soignard, K. A. McKiernan, C. J. Benmore, J. L. Yarger, *Solid State Commun.* **2012**, 152, 390.

[15]   N. B. Hannay, Springer US, 1976.

[16]   a) M. E. Paulaitis, J. M. L. Penninger, R. D. Gray, Eds., *Chemical Engineering at Supercritical Fluid Conditions*, Ann Arbor Science Publishers, 1983; b) J. A. Darr, M. Poliakoff, *Chem. Rev.* **1999**, 99, 495.

[17]   B. D. Largy, A. Finch, P. J. Gardner, N. Kell, *J. Chem. Soc. Faraday Trans. 1* **1983**, 79, 383.

[18]   a) X. S. Zhou, L. J. Wan, Y. G. Guo, *Adv. Mater.* **2013**, 25, 2152; b) W. Li, F. Wang, S. Feng, J. Wang, Z. Sun, B. Li, Y. Li, J. Yang, A. A. Elzatahry, Y. Xia, D. Zhao, *J. Am. Chem. Soc.* **2013**, 135, 18300.

[19]   a) X. Rui, X. Zhao, Z. Lu, H. Tan, D. Sim, H. H. Hng, R. Yazami, T. M. Lim, Q. Yan, *ACS Nano* **2013**, 7, 5637; b) P. Xiong, B. Liu, V. Teran, Y. Zhao, L. Peng, X. Wang, G. Yu, *ACS Nano* **2014**, 8, 8610; c) H. Wang, H. Yuan, S. Sae Hong, Y. Li, Y. Cui, *Chem. Soc. Rev.* **2015**, 44, 2664.

[20]   a) F. Bonaccorso, L. Colombo, G. Yu, M. Stoller, V. Tozzini, A. C. Ferrari, R. S. Ruoff, V. Pellegrini, *Science* **2015**, 347, 1246501; b) S. K. Das, R. Mallavajula, N. Jayaprakash, L. A. Archer, *J. Mater. Chem.* **2012**, 22, 12988; c) D. Chen, H. Feng, J. Li, *Chem. Rev.* **2012**, 112, 6027; d) Z.-S. Wu, W. Ren, L. Xu, F. Li, H.-M. Cheng, *ACS Nano* **2011**, 5, 5463; e) S. Y. Yin, Y. Y. Zhang, J. H. Kong, C. J. Zou, C. M. Li, X. H. Lu, J. Ma, F. Y. C. Boey, X. D. Chen, *ACS Nano* **2011**, 5, 3831; f) S. Yang, R. E. Bachman, X. Feng, K. Müllen, *Acc. Chem. Res.* **2013**, 46, 116.

[21]   a) Y. Tang, Y. Zhang, W. Li, B. Ma, X. Chen, *Chem. Soc. Rev.* **2015**, 44, 5926; b) Y. Tang, Y. Zhang, J. Deng, J. Wei, H. L. Tam, B. K. Chandran, Z. Dong, Z. Chen, X. Chen,

Adv. Mater. **2014**, 26, 6111; c) Y. Tang, Y. Zhang, J. Deng, D. Qi, W. R. Leow, J. Wei, S. Yin, Z. Dong, R. Yazami, Z. Chen, X. Chen, *Angew. Chem. Int. Ed.* **2014**, 53, 13488; d) Y. Tang, Y. Zhang, X. Rui, D. Qi, Y. Luo, W. R. Leow, S. Chen, G. Jia;, J. Wei, W. Li, J. Deng, Y. Lai, B. Ma, X. Chen, *Adv. Mater.* **2015**, 27, Doi: 10.1002/adma.201505161; e) C. Wu, X. Lu, L. Peng, K. Xu, X. Peng, J. Huang, G. Yu, Y. Xie, *Nat. Commun.* **2013**, 4, 2431; f) Y. Xu, Z. Lin, X. Zhong, X. Huang, N. O. Weiss, Y. Huang, X. Duan, *Nat. Commun.* **2014**, 5, 4554.

[22] X. H. Rui, N. Ding, J. Liu, C. Li, C. H. Chen, *Electrochim. Acta* **2010**, 55, 2384.
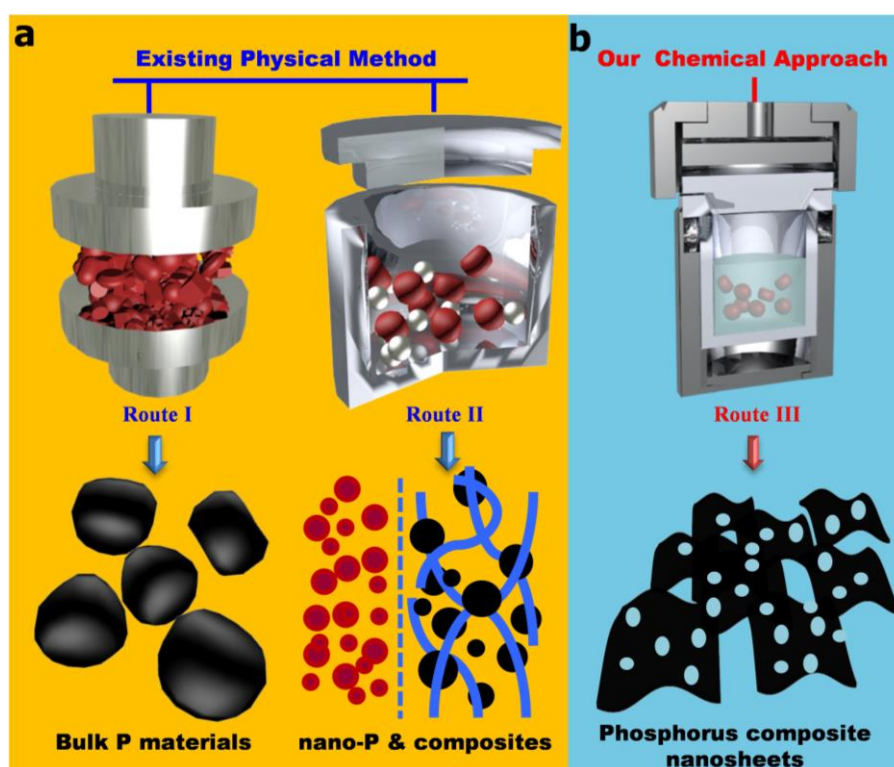
Scheme 1. Schematic illustration of the formation of phosphorus-based materials. (a) Existing physical solid-state methods: Route (I) for the formation of bulk black P materials by traditional high-pressure method; Route (II) for the formation of nanosized (left) P material or its nanocomposites (right; carbon-, metal-composite, etc.) via normal/high-energy mechanical milling methods. (b) Our chemical approach: Route (III) for the preparation of holey phosphorus-based composite nanosheets via a chemical solvothermal reaction.
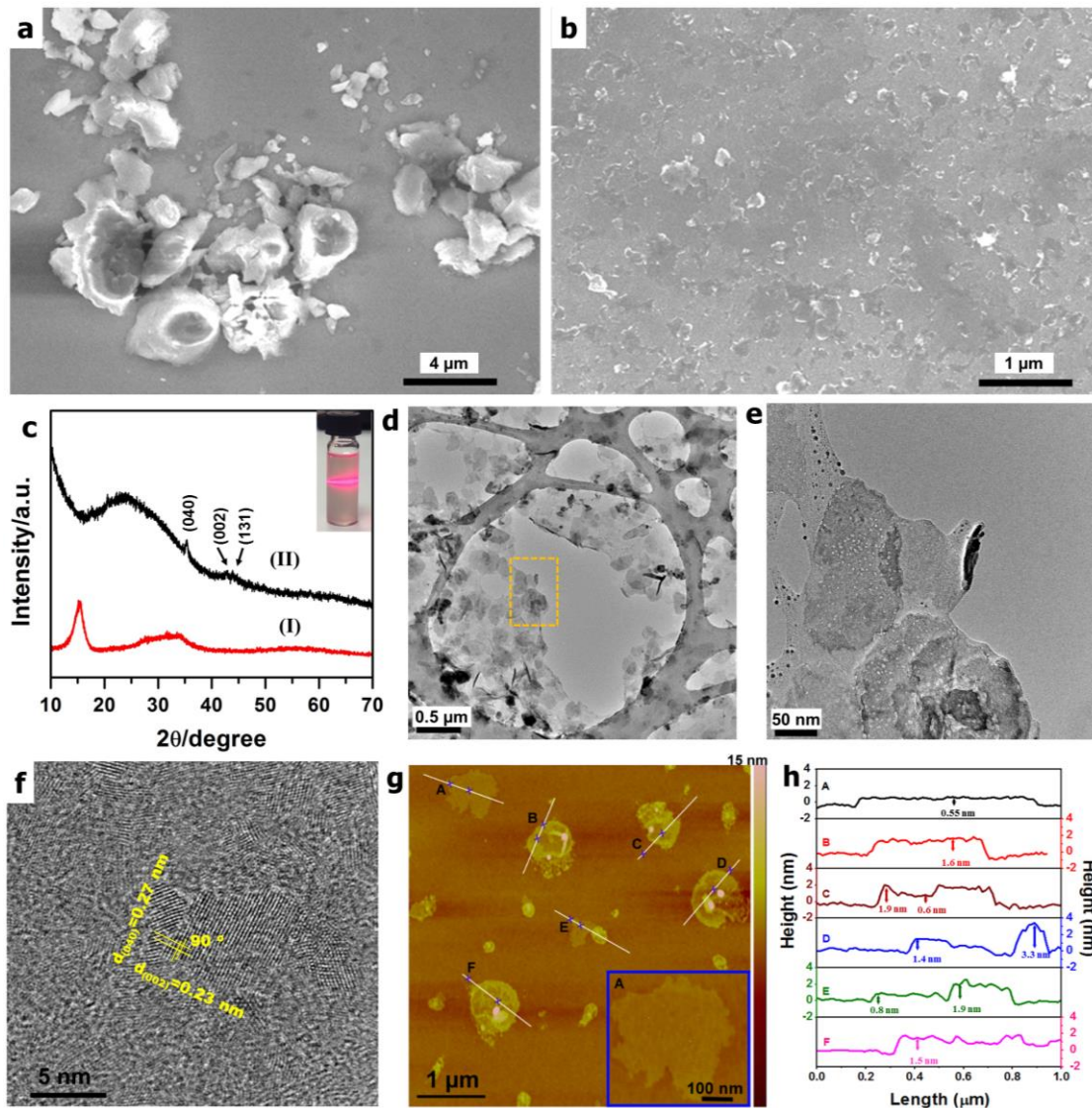
Figure 1. (a) FESEM images of (a) red phosphorus precursor and (b) the synthesized phosphorus composite nanosheets. (c) XRD patterns of (I) red phosphorus and (II) phosphorus-based nanosheets. The marked peaks belong to orthorhombic phase of black phosphorus. The inset is the diluted phosphorus composite nanosheets in ethanol solution. (d-e) Low-magnification of TEM images of the holey phosphorus-based nanosheets. (f) HRTEM image of phosphorus-based nanosheets, showing the amorphous regions with some polycrystalline structure; (g) AFM image and (h) the corresponding heights of the nanosheets marked in (g).
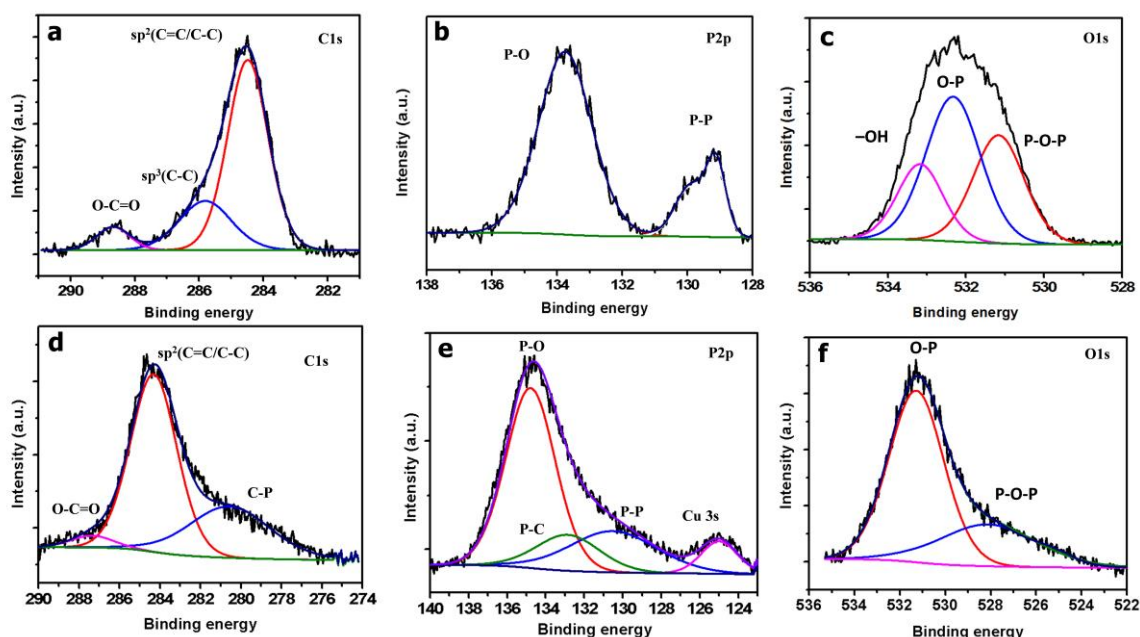
Figure 2. Fine scanning XPS spectra of C1s, P2p, O1s peaks for commercial red phosphorus (a-c) and phosphorus-based composite nanosheets (e-f) after solvothermal reaction, confirming the formation of the P-O peak. All spectra are calibrated to the binding energy of adventitious carbon (284.5 eV). The carbon signal of red P in (a) comes from the carbon tape or the carbon impurities in XPS vacuum chamber, while the carbon signal in (d) is originated from the phosphorus-based composite nanosheets. The peak shift for phosphorus element in (b, d) is due to the different oxidation state. The Cu3s peak in (e) is generated from the copper foil substrate for the XPS measurement.
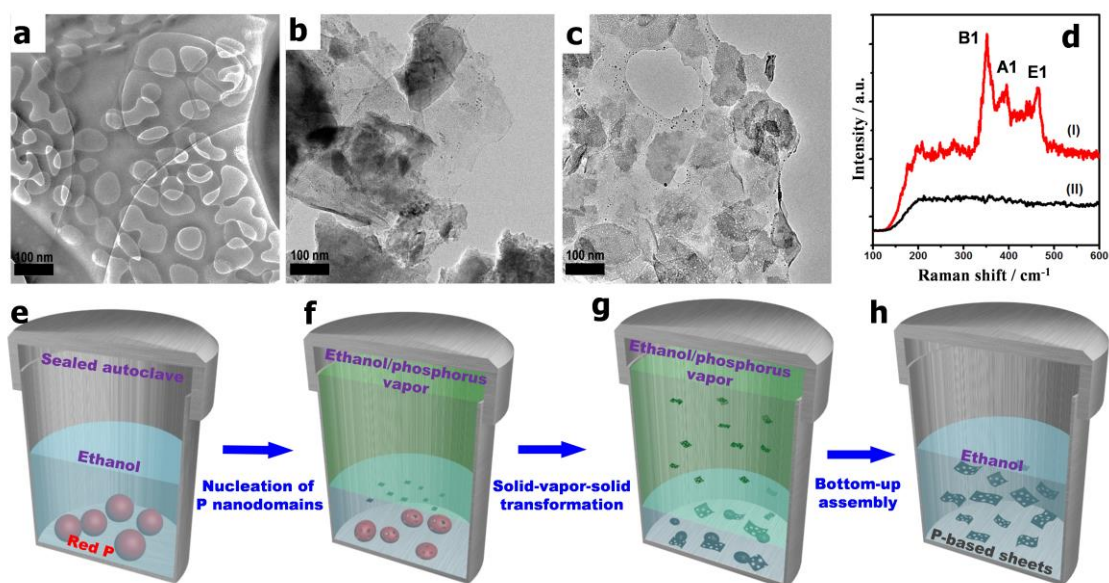
Figure 3. The morphology evolution of the bulk red phosphorus materials during the high-temperature solvothermal reaction at different reaction time: (a) 2 h; (b) 12 h; and (c) 24 h. (d) Raman spectra of (I) the precursor and (II) the final products. Proposed formation schematics of the holey phosphorus composite nanosheets: (e) sublimation of the red phosphorus bulk materials, (f) formation of phosphorus nanodomain in ethanol solution (ethanol/phosphorus vapor on the top) at the initial stage, (g) the formation of phosphorus nanosheets in the ethanol vapor (near supercritical fluid) by bottom-up assembly process, and (h) the resulted product in ethanol solution eventually.
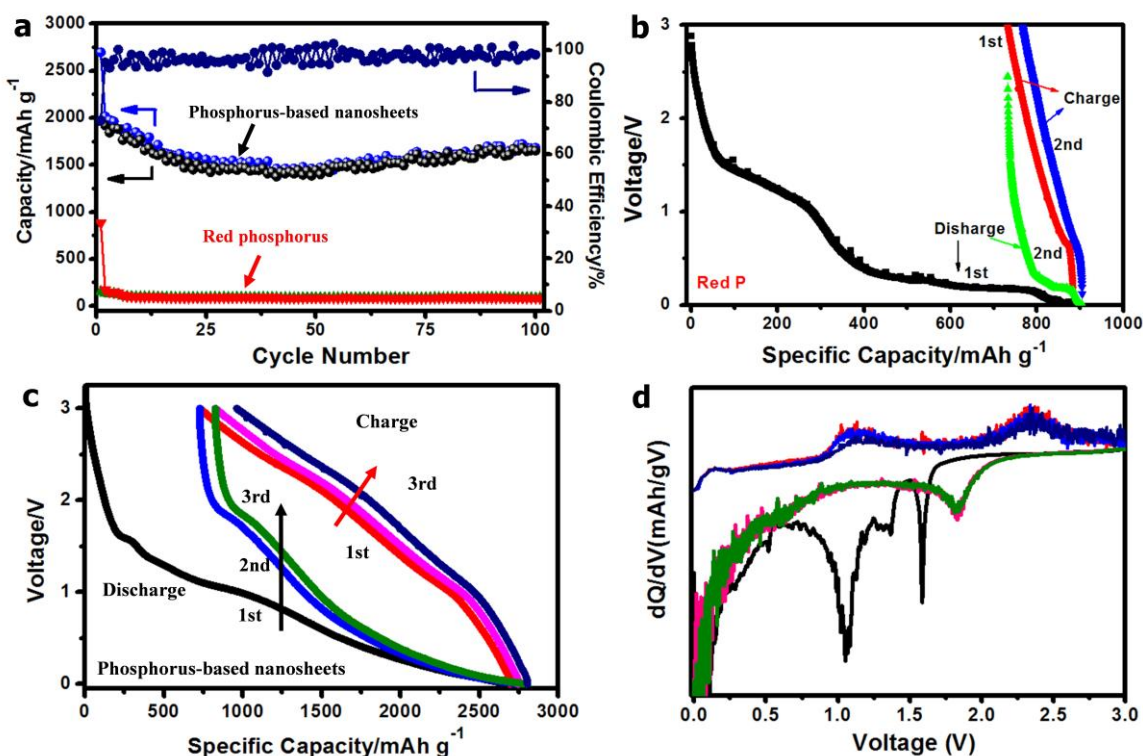
Figure 4. (a) Cycle performance comparison of phosphorus composites nanosheets and red phosphorus materials at a current density of 0.2 A/g; (b) Voltage profiles of red phosphorus and (c) phosphorus composites nanosheets at 0.2 A/g respectively; and (d) is the associated derivative –*dQ/dV* plot from (c). In (d), a continuous reduction potential is observed below 1.0 V (with the oxidation peak at ca. 0.1, 1.1 V) and a stable reduction peak at ca. 1.8 V (with oxidation peak at 2.3 V) are observed for phoshours composites nanosheet samples.
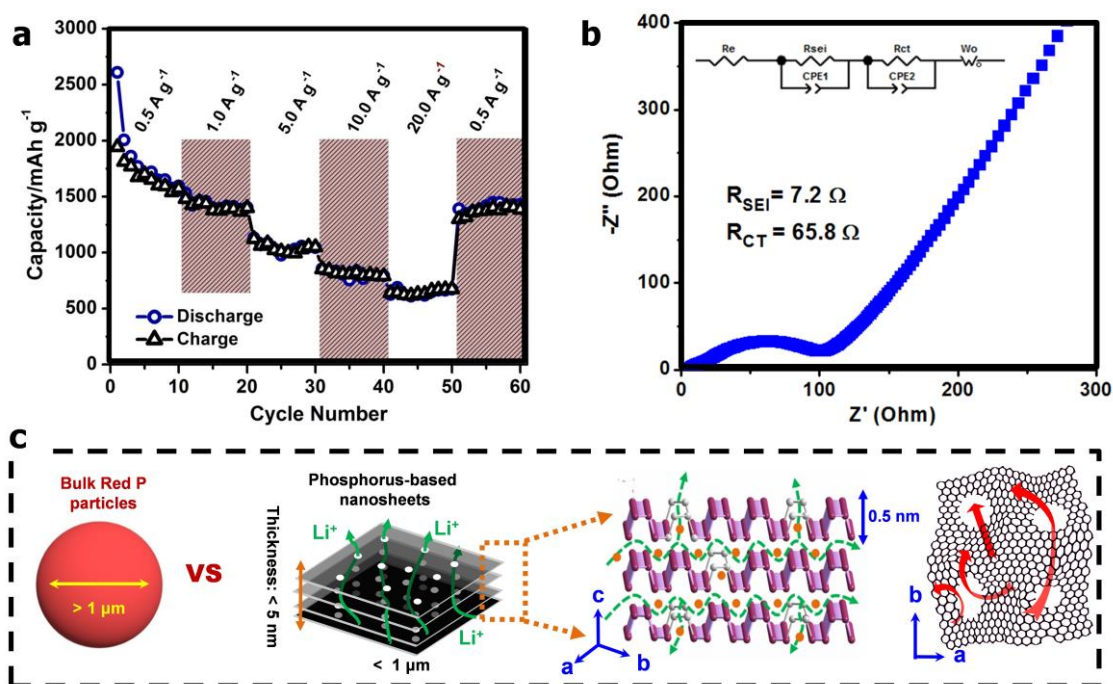
Figure 5. (a) Rate capability of phosphorus-based nanosheets at different current density. (b) Electrochemical impedance spectroscopy (Amplitude: 5 mV, 1 MHz~0.01 Hz) of nanosheets electrode. (c) Schematic of lithiation/delithiation processes for the bulk red phosphorus and holey phosphorus nanosheets. The nanopores in holey phosphorus composite sheets provide lithium ion sources reservoir for neighbored layers of phosphorus to greatly speed up the ion transport across the entire film. The two crystal models in the bottom of (c) are the lithium ion diffusion pathways in the layered phosphorus composite nanosheets (left) and in the single layer of holey amorphous phosphorus (right) respectively.

The table of contents entry

We have developed a sublimation-induced synthesis strategy to form holey phosphorus-based composite nanosheets by a chemistry-based solvothermal reaction. As proof-of-concept, the phosphorus composite nanosheets electrodes can achieve a high capacity of 630 mAh/g at ultrahigh current density of 20 A/g.

Keywords: Phosphorus composite nanosheets, lithium-ion batteries, anode materials, high-rate, solvothermal reaction

Yanyan Zhang, Xianhong Rui, Yuxin Tang, Yaqing Liu, Jiaqi Wei, Shi Chen, Wan Ru Leow, Wenlong Li, Yuanjun Liu, Jiyang Deng, Bing Ma, Qingyu Yan,* Xiaodong Chen*

Wet-Chemical Processing of Phosphorus Composite Nanosheets for High-Rate and High-Capacity Lithium-ion Batteries

TOC Figure